Table 1 Specifications of inclined centrifuge microscope

Angle of microscope	θ_0	0–50 deg
Angle of base plate	θ	40–90 deg
Angular frequency	ω	0–1257 rad/s
Magnification on 17 in monitor (10× and 50× objective lens)		×255, ×1275
Rotation radius	r_0	5.43×10^{-2} m
Rotation speed	N	0–12,000 rpm

Table 2 Physical properties of specimen

Erythrocytes	
Diameter d_r	8.4×10^{-6} m
Height h_r	2.4×10^{-6} m
Volume V_r	8.7×10^{-17} m^3
Density ρ_r	1087 kg/m^3
Plasma	
Density ρ_p	1025 kg/m^3
Viscosity μ_p	1.2×10^{-3} Pa s
Saline	
Density ρ_s	998.2 kg/m^3
Viscosity μ_s	1.01×10^{-3} Pa s

processed by the PTV software program (Nexus, PIV EXPERT 2000) to obtain the velocity vectors of the erythrocytes. After the removal of background noise and smoothing, centers of gravity of all erythrocytes were obtained. The particle tracing velocimetry method was then applied in order to determine the velocity vectors of all the cells based on the distribution of cell centers at two time instants. The cell velocity is evaluated by the velocity component parallel to the tangential force since the rotational velocity component is strongly affected by the fluctuation in synchronization.

2.2 Principle of Friction Force Measurement. A schematic of the sample container is shown in Fig. 3. The plate is placed at the bottom of the container, which is inclined at an angle of θ from the horizontal plane (Fig. 3(*a*)). The container is filled with a medium (plasma or saline) in which erythrocytes have been dispersed. By applying rotation at an angular velocity ω, the cells move in a radial direction under the effect of centrifugal force F described as

$$F = (\rho_r - \rho_m)V_r r_0 \omega^2 \tag{1}$$

where ρ_r, ρ_m are the densities of the erythrocyte and the medium, respectively, V_r is the volume of the cell (Table 2), and r_0 is the rotation radius (Table 1). Note that we consider the case in which the effect of gravitation is negligible and the rotation radius is assumed to be constant. After the cells contact the plate, the centrifugal force on each cell is naturally divided into two components; the normal force F_N and the tangential force F_T (Fig. 3(*b*)) as

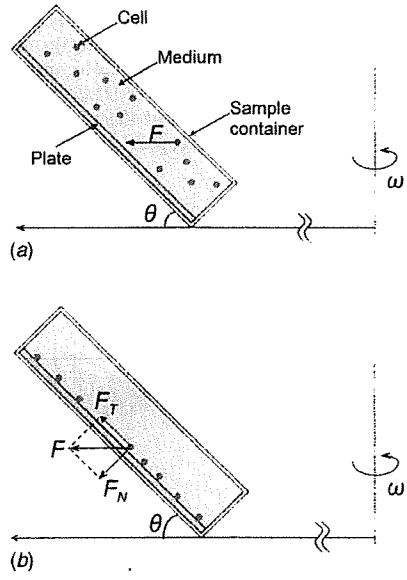

Fig. 3 Principle of friction force measurement in a rotating field: (*a*) initial state and (*b*) steady-state movement of erythrocytes

$$F_N = F\sin\theta, \quad F_T = F\cos\theta \tag{2}$$

The normal force F_N balances the reaction from the plate, and the tangential force F_T accelerates the cell along the plate. When the cell velocity U reaches a steady value, the tangential force F_T is equal to the sum of the friction force F_T^* from the plate and the drag force f_D from the medium above the cell as

$$F_T = F_T^* + f_D \tag{3}$$

Precisely modeling the drag force for the shape of an actual erythrocyte is difficult. Since the Reynolds number based on the diameter and velocity of the cell and on the kinematic viscosity of the medium is less than 10^{-3} for the condition examined in the present study, we use the drag coefficient C_D of the Stokes equation for a sphere [12].

$$f_D = C_D(h_r d_r)\frac{1}{2}\rho U^2, \quad C_D = 24/R_e \tag{4}$$

where h_r and d_r denote the height and the diameter of the erythrocyte, respectively (Table 2).

As the force components F_N and F_T are specified arbitrarily by adjusting the angle of the container θ and the angular velocity ω, measuring the cell velocity U for a variety of force conditions gives the friction characteristics of the erythrocytes moving along the plate. A finite time is required before the cells attain a steady velocity with all forces in equilibrium.

By the assumption that the friction force is approximately described as the viscous friction of the uniform shear flow between the cell and the plate, we have the following equation:

$$F_T^* = \mu \cdot \dot{\gamma} \cdot \pi d_r^2/4 \tag{5}$$

where $\dot{\gamma}$ is the equivalent shear rate of the flow in a gap between the cell and the plate. The equivalent gap width h_e is given as

$$h_e = U/\dot{\gamma} \tag{6}$$

3 Materials and Methods

Human venous blood was sampled to a vacuum blood-collecting vessel (NIPRO NEO TUBE PET) from an informed healthy male volunteer of 24 years old. The blood anticoagulated by citric acid sodium (3.13%) was centrifuged (1000 g, 10 min) to separate plasma and erythrocytes. The plasma was centrifuged again in the same manner to purify it. A separate plasma and saline were then prepared as two mediums. Separated erythrocytes were distributed in the mediums at a volumetric concentration of 0.01%. The *p*H of the sample was 7.5 ± 0.1. The experiment was performed within 6 h after blood sampling and at a constant room temperature of 20 ± 1 °C. The physical properties of the materials are summarized in Table 2. The density of erythrocytes and that of the plasma are referred from our former study [9], whereas the other properties were obtained from literature [13].

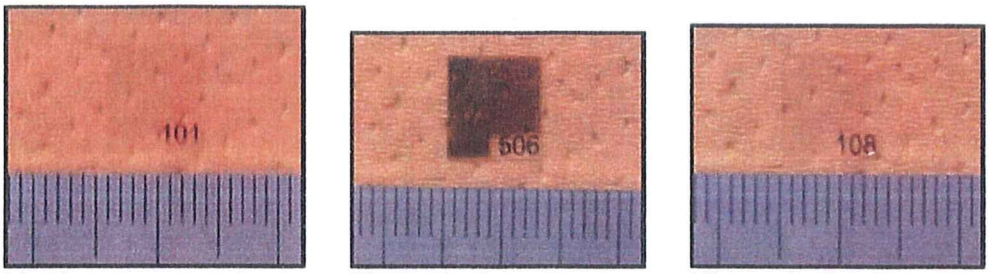

(a) (b) (c)

Fig. 4 Sample plates (small division=1 mm): (*a*) MPC-coated plate, (*b*) DLC-coated plate, and (*c*) non-coated plate

Pieces of cover glass made of synthetic quartz (Takahashi Giken Glass, 0.15 mm thickness) were used as the plates. Some of them were coated with DLC or MPC polymer. DLC coating was fabricated by chemical vapor deposition (CVD) technique. The deposition was performed for 20 min under the condition of 2.2 $\times 10^{-2}$ torr and -700 V of substrate self-bias voltage. A methane gas was used as a precursor gas. MPC polymer was coated on a different plate by putting the plate into PMB ethanol solution (0.2 wt %) and drying it naturally. The PMB ethanol is a mixture of non-water-soluble PMB30 and water-soluble PMB80 in a ratio of 9:1.

Figure 4 shows photographs of (*a*) a glass plate coated with MPC polymer (MPC-coated plate), (*b*) a glass plate coated with DLC (DLC-coated plate), and (*c*) a glass plate without coating (noncoated plate), respectively. The MPC-coated plates look the same as the noncoated plates. The DLC-coated plates are colored light brown but transparent.

Surface roughness of a noncoated plate and a DLC-coated plate was measured with an atomic force microscopy (AFM) (Veeco Enviroscope equipped with the NanoScope IV Controller). As shown in Fig. 5 the DLC-coated plate has larger roughness than the noncoated plate, but is still very smooth with roughness less than 10 nm. Since the probe used in the measurement was not applicable to soft surfaces, the surface roughness of MPC-coated plates was not measured.

4 Results

The motion of the erythrocytes on the three kinds of plates was first observed by using the 50× objective lens of the inclined centrifuge microscope. The friction characteristics were then measured by the 10× objective lens. In the experiment, tangential force component F_T was set between 2.5 pN and 40 pN while maintaining the normal force component F_N at 47 pN.

Figure 6 shows a snapshot of a motion picture in which erythrocytes (large circles) are moving upward in the figure on the MPC-coated plate in the medium of plasma under the effect of centrifugal force with a tangential force component F_T of 35 pN and a normal force component F_N of 47 pN. As mentioned above the tangential force component drives the cells to move on the plate and the normal force component pushes the cells on the plate. In the figure, the configurations of erythrocytes are clearly defined including a dark part in the center corresponding to a typical concave shape. The small dots in the figure are most likely aggregations of fibrinogen in plasma. Similar results were obtained for the noncoated plate and the DLC-coated plate under the same conditions.

For a relatively small tangential force of F_T=5 pN, some differences appear in the motion of erythrocytes between the plates. All the cells move on the MPC-coated plate, but some cells rest on the noncoated plate and more cells rest on the DLC-coated plate. The velocity of cells on the MPC-coated plate was larger than that of the others. The motion of moving cells on the DLC-coated plate fluctuated in a transverse direction in comparison with the other cases.

We then replaced plasma with saline as the medium. Figures 7(*a*) and 7(*b*) show the results for the MPC-coated and the DLC-coated plates, respectively, where F_T=30 pN and F_N=47 pN. Cells on the MPC-coated plate move smoothly but those on the DLC-coated plate stick to the plate stretching in the tangential force direction due to centrifugal force. The results of the noncoated plate were similar to that of the DLC-coated plate.

Next we measured the velocities of the cells to evaluate the friction characteristics of erythrocytes on the plates. In order to

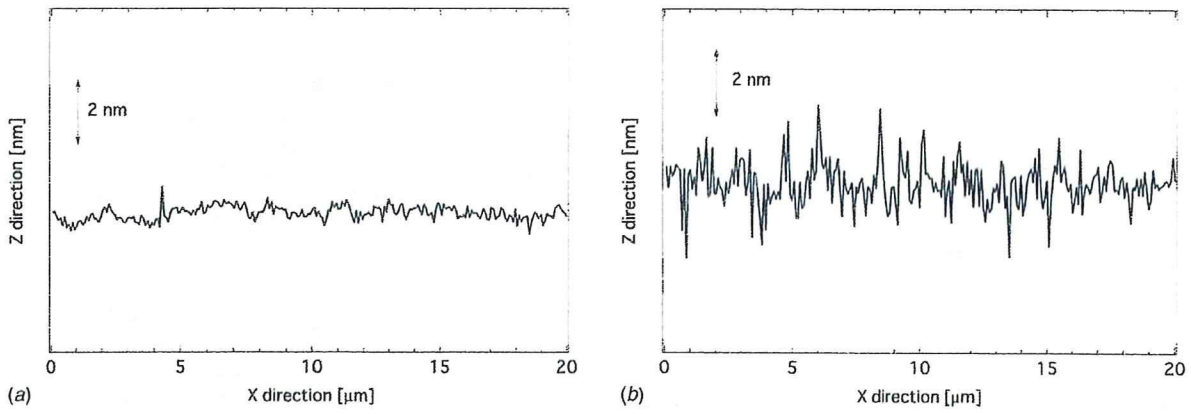

Fig. 5 Roughness of sample plates measured by AFM: (*a*) noncoated plate and (*b*) DLC-coated plate

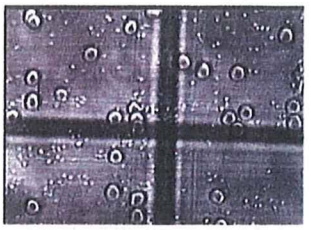

Fig. 6 Behavior of erythrocytes in plasma on MPC-coated plate (F_T=35 pN, F_N=47 pN)

observe a sufficient number of cells we used the 10× objective lens. The normal force was fixed at F_N=47 pN and the tangential force F_T was set at 5 pN intervals between 5 pN and 40 pN using plasma as a medium on the MPC-coated, DLC-coated, and noncoated plates, and at F_T=2.5, 5, 10, 20, 30 pN using saline as a medium on the MPC-coated plate.

Figure 8 is an example of 1 of 100 sequentially captured images for F_T=35 pN using plasma on the noncoated plate. These images were processed by the PTV software to obtain the velocities of cells using two sequential images. The typical number of velocities of cells obtained on the image was 140 in the present work. The mean value and the standard deviation of the velocities of cells obtained in each image are plotted in Figs. 9(*a*) and 9(*b*), respectively. By averaging these data we obtained the mean value and the standard deviation of the cell velocities for one experimental condition.

Figures 10(*a*)–10(*c*) show the mean velocity of cells with the tangential force for the MPC-coated, DLC-coated, and noncoated plates, respectively. The open symbol represents the results for plasma as the medium, while the closed symbol in Fig. 10(*a*) represents the results for saline. Each plot is based on the average value of four measurements of the same blood sample. For the plasma medium, the measurement was performed more than once using the blood of the same person sampled on different days. A pair of plots at the same F_T in a range of 10–40 pN represent the results three months apart. There are no data with saline as a medium for DLC-coated and noncoated plates since all the cells stick to the plates under this condition.

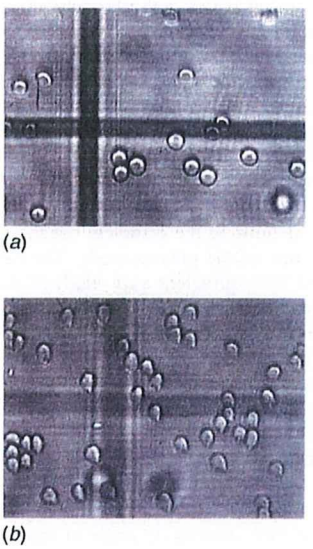

(*a*)

(*b*)

Fig. 7 Behavior of erythrocytes in saline (F_T=30 pN, F_N =47 pN): (*a*) MPC-coated plate and (*b*) DLC-coated plate

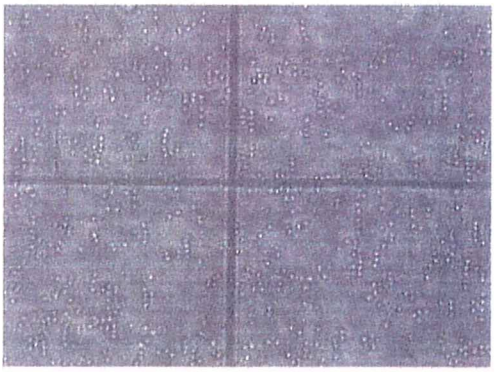

Fig. 8 Behavior of erythrocytes in plasma on noncoated plate (F_T=30 pN, F_N=47 pN).

By introducing the above results into Eq. (3), we obtained the friction force working between the cells and the plate. Equivalent shear rate and gap width were obtained from Eqs. (5) and (6). Figure 11(*a*) shows the friction force and the equivalent shear rate as a function of the mean cell velocity for the MPC-coated, DLC-coated, and noncoated plates in plasma and the MPC-coated plate in saline. Figure 11(*b*) shows the corresponding results for the equivalent gap width.

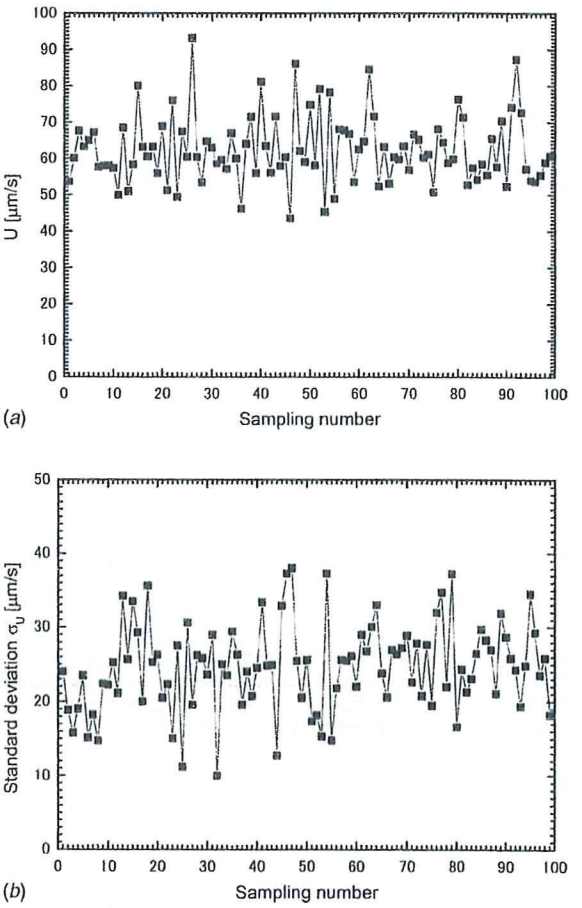

Fig. 9 Variation of mean value and standard deviation of velocity of erythrocytes in plasma on noncoated plate (F_T =30 pN, F_N=47 pN): (*a*) mean value and (*b*) standard deviation

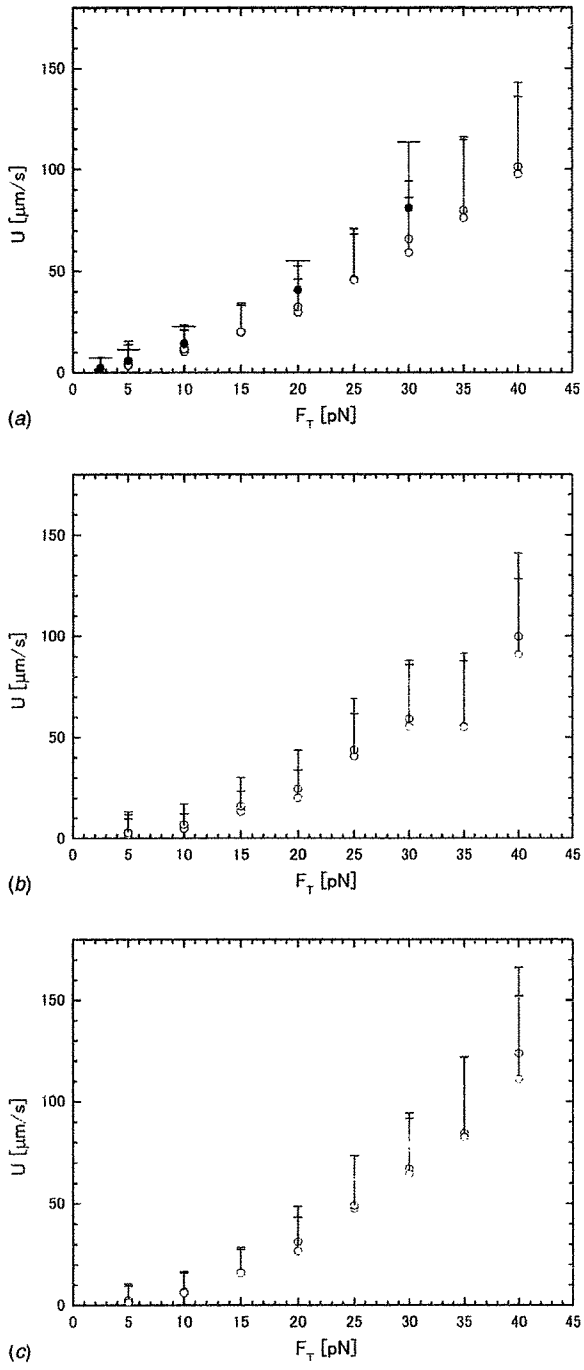

Fig. 10 Cell velocity in plasma with tangential force. Open symbols: plasma; closed symbols: saline; error bar represents standard deviation. (F_N=47 pN): (*a*) MPC-coated plate, (*b*) DLC-coated plate, and (*c*) noncoated plate.

5 Discussion

Under magnification, the typical concave configuration of erythrocytes was clearly observed. It is well known that a tank-treading motion sometimes occurs for erythrocytes in a shear flow [14] or for those moving eccentrically in a capillary [15]. In the present experiment, occurrence of the tank-treading motion was examined in movies by observation of face-on outline of cells. Such observation indicated that the cells move without tank treading motion as the face-on outlines distorted from circular shape do not change during the motion. The centrifugal force is applied to the entire body of each cell, or equivalently to its gravitational center and shear force around the cell balances the centrifugal force. The shear force on the bottom surface of the cell dominates in the total shear force while that on the top surface is small but has the same direction as that of the bottom surface. For a cell in a shear flow, on the other hand, shear forces acting on the top and bottom sides of the cell at the same magnitude and in opposite directions effectively drive the cell into a tank-treading motion. However, a recent study suggests that a tank-treading motion can occur on a cell in a biconcave shape at low shear stress [16]. Therefore, it is necessary to exactly identify the occurrence of tank-treading motion under the present experimental conditions, for example, by marking a certain location on the cell surface with latex spheres in a future study.

The friction characteristics of erythrocytes in plasma using the DLC-coated and noncoated plates are similar changing approximately proportional to the 0.5th power of the cell velocity. The cells stick to the plates when plasma is replaced with saline, implying that plasma protein plays an important role to determine friction characteristics. The results of the MPC-coated plate using plasma are similar to those using the other plates in the range of relatively large cell velocity, but deviate from those with decreased cell velocity. The results change nearly proportional to the 0.75th power of the cell velocity in the range of small velocities less than 10 μm/s. The friction force observed in the MPC-coated plate in saline is similar to that in plasma but somewhat smaller. This means that the friction characteristics of cells using the MPC-coated plate are essentially independent of plasma protein. Therefore, in the range of large cell velocities, in which all the friction characteristics are similar, plasma protein plays a secondary role in determining friction characteristics.

Shear stress in the fluid flow between the cell and the plate should play the essential role to determine the friction force. The cell velocity, the gap width between the cell and the plate, and the viscosity of the fluid are the factors that determine the flow shear stress. The shear rate in the gap ranged between 30 1/s and 700 1/s in a present experiment. It should be noted that the resultant shear force acted only on the bottom surface of the cell to counterbalance the centrifugal force. Therefore, the effect of this shear rate on the cell motion is different from that on a cell in a uniform shear flow. The equivalent gap distance between the cell and the plate ranged between 0.02 μm and 0.2 μm. The results for the MPC-coated plates with plasma and saline were identical. The gap widths for the DLC-coated and noncoated plates were almost the same and were smaller than those of MPC-coated plates. In a previous study [9], we proposed that the distance corresponds to the size of plasma protein, but the present result for the MPC-coated plate with saline invalidates this possibility. Electrochemical force, such as the strong attraction of water molecules on the surface of MPC polymer [11], or hydrodynamic force, such as squeezing force due to the movement of the cell, should be considered to determine the distance, but these considerations go beyond the scope of the present study. The deviation of the friction force and the equivalent gap width of the DLC-coated and noncoated plates from that of the MPC-coated plate in small velocities is probably explained by the effect of additional friction force due to plasma proteins.

In circulatory medical devices, centrifugal force acts on the blood flow in a curved duct or in a turbo pump. In such a case blood cells are forced to move along a device surface under the effect of normal forces. The present findings suggest that friction force acting on the erythrocytes on the MPC-coated plate is smaller than that on the DLC-coated or noncoated plate in the region of small cell velocity. In order to apply these results to the device design, however, further study is necessary, for example, clarification of the effect of normal force or temperature. It is also important to evaluate the normal force acting on blood cells in a

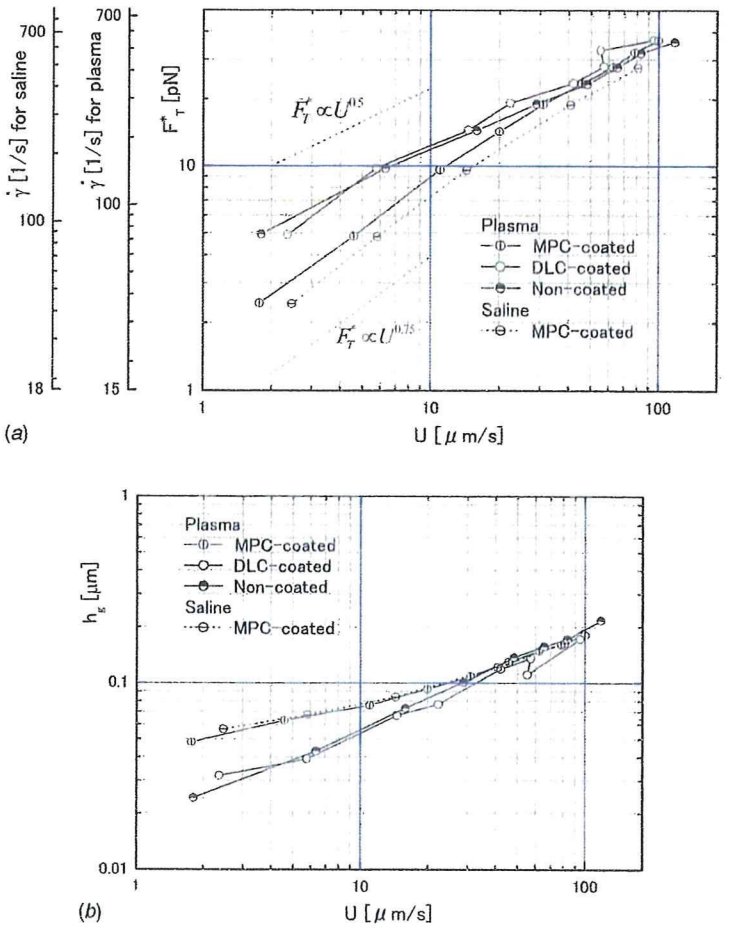

Fig. 11 Friction characteristics of erythrocytes: (*a*) friction and equivalent shear rate and (*b*) equivalent gap width

blood flow. Relating to this problem, although theoretical work has been performed for the Stokes flow impinging on a spherical cap on a plane wall [17], further study must be done. Frictional characteristics between blood cells and device surfaces are important for hemolysis and thrombosis. The present study dealt with the frictional characteristics of erythrocytes in relation to hemolysis in the devices as the first step. For thrombosis in medical devices, consideration of platelets is essential. Application of the present method to platelets and other cells such as neutrophils will be treated in a future work.

In addition, we would like to mention that the friction characteristics of erythrocytes moving along a flat plate under the inclined centrifugal force differ from those of the blood flow in blood vessels. However, the present method provides a fundamental understanding of the frictional characteristics of blood cells, providing a basis upon which a mathematical model of microcirculation can be constructed. For that purpose, measurements using endothelial-cell-cultured glass plates are a natural extension of the present research.

Acknowledgment

The authors acknowledge Professor Toshiyuki Takagi of the Institute of Fluid Science, Tohoku University for his help in making the DLC-coated plates, and Professor Kazuhiko Ishihara of the University of Tokyo for providing MPC polymer and for useful discussions. They wish to thank the staff of Department of Radiology and Health Administration Center, Tohoku University for their assistance in blood sampling. They also thank Mr. Manabu Saito for his help in preparing the manuscript.

References

[1] Schmid-Schoenbein, G. W. 1999. "Biomechanics of Microcirculatory Blood Perfusion," Annu. Rev. Biomed. Eng., **1**, pp. 103–127.
[2] Pries, A. R., Secomb, T. W., and Gaehtgens, P., 2000. "The Endothelial Surface Layer," Eur. J. Physiol., **440**, pp. 653–666.
[3] Secomb, T. W., Hsu, R., and Pries, A. R., 1998. "A Model for Red Blood Cell Motion in Glycocalyx-Lined Capillaries," Am. J. Physiol. Heart Circ. Physiol. **274**(3), pp. H1016–H1022.
[4] Harvey, E. N., and Loomis, A. L., 1930, "Scientific Apparatus and Laboratory Methods," Science, **72**, pp. 42–44.
[5] Inoue, S., Knudson, R. A., Goda, M., Suzuki, K., Nagano, C., Okada, N., Takahashi, H., Ichie, K., Iida, M., and Yamanaka, K., 2001. "Centrifuge Polarizing Microscope. I. Rationale, Design and Instrument Performance," J. Microsc., **201**, pp. 341–356.
[6] Kaneda, I., Kamitsubo, E., and Hiramoto, Y., 1990. "The Mechanical Structure of the Cytoplasm of the Echinoderm Egg Determined by 'Gold Particle Method' Using a Centrifuge Microscope," Dev., Growth Differ., **32**, pp. 15–22.
[7] Kuroda, K., and Kamiya, N., 1989. "Propulsive Force of Paramecium as Revealed by the Video Centrifuge Microscope," Exp. Cell Res., **184**, pp. 268–272.
[8] Tameyasu, T., Akimoto, T., Hirohata, Y., Shirakawa, I., Yamamoto, N., Kosuge, S., and Sugi, H., 1998. "Force-Velocity Relation of Sliding of Skeletal Muscle Myosin, Arranged on a Paramyosin Filament, on Actin Cables," Jpn. J. Physiol., **48**, pp. 115–121.
[9] Hayase, T., Shirai, A., Sugiyama, H., and Hamaya, T., 2002. "Measurement of Frictional Characteristics of Red Blood Cells Moving on a Plate in Plasma Due to Inclined Centrifugal Force (in Japanese)," Trans. Jpn. Soc. Mech. Eng., Ser.

B, **68**, pp. 3386–3391
[10] Mohanty, M. Anilkumar, T. V., Mohanan, P. V., Muraleedharan, C. V., Bhuvaneshwar, G. S., Derangere, F., Sampeur, Y., and Suryanarayanan, R., 2002, "Long Term Tissue Response to Titanium Coated With Diamond Like Carbon," Biomol. Eng., **19**, pp. 125–128.
[11] Ishihara, K., Nomura, H., Mihara, T., Kurita, K., Iwasaki, Y., and Nakabayashi, N., 1998, "Why do Phospholipid Polymers Reduce Protein Adsorption?," J. Biomed. Mater. Res., **39**, pp. 323–330.
[12] Schlichting, H., 1979, *Boundary-Layer Theory*, 7th English ed. McGraw-Hill, New York, p. 114.
[13] Cooney, D. O., 1976, *Biomedical Engineering Principles: An Introduction to Fluid, Heat, and Mass Transport Process*, Dekker, New York.
[14] Sutera, S. P., Tran-Son-Tay, R., Boylan, C. W., Williamson, J. R., and Gardner, R. A., 1983, "A Study of Variance in Measurements of Tank-Treading Frequency in Populations of Normal Human Red Cells," Blood Cells, **9**, pp. 485–495.
[15] Fung, Y. C., 1996, *Biomechanics: Circulation*, Springer-Verlag, New York, p. 308.
[16] Fischer, T. M., 2004, "Shape Memory of Human Red Blood Cells," Biophys. J., **86**, pp. 3304–3313.
[17] El-Kareh, A. W., and Secomb, T. W., 1996, "Stokes Flow Impinging on a Spherical Cap on a Plane Wall," Q. J. Mech. Appl. Math., **49**, pp. 179–193.

Journal of Biomechanical Science and Engineering

Vol. 3, No. 2, 2008

Experimental Validation of Color Doppler Velocity Measurement for Ultrasonic-Measurement-Integrated Simulation of Blood Flow*

Lei LIU**, Toshiyuki HAYASE***, Makoto OHTA*** and Kosuke INOUE***

** Graduate School of Engineering, Tohoku University, Aramaki Aza Aoba, Aoba-ku, Sendai, JAPAN

E-mail: ryu@reynolds.ifs.tohoku.ac.jp

*** Institute of Fluid Science, Tohoku University, Katahira, Aoba-ku, Sendai, JAPAN

Abstract

Cardiovascular diseases are closely related to blood flow. Ultrasonic-Measurement-Integrated (UMI) simulation, in which results of ultrasonic measurement are fed back to the flow simulation, was proposed in a previous study in order to reproduce the real blood flow accurately and efficiently. The usability of the UMI simulation was confirmed by numerical experiment, but the effectiveness of this simulation was strongly affected by the accuracy of the ultrasonic measurement. In this paper, we examined the accuracy of a commercial ultrasonic measurement device by an experiment with a PVA-H straight tube phantom. By analyzing the measured color Doppler images for a developed laminar flow inside the phantom, we obtained the relationship between the color Doppler value and the Doppler velocity (C-V relationship). It was revealed that the original C-V relationship provided in the device as a color bar was not suitable for quantitative evaluation of Doppler velocity to be used in UMI simulation. Compared with the original C-V relationship, the present C-V relationship results are in far better agreement with the analytic solution. Investigation of the normalized error confirmed that the result obtained with the present C-V relationship was reliable in cases of relatively high Reynolds number in the flow domain except near the wall. The two signal conditioning factors of the device had little influence on the Doppler velocity. Finally, we investigated the effect of temporal and spatial averaging of ultrasonic measurement data to clarify the relation between the number of averagings and the level of agreement with the analytic solution.

Key words: Ultrasonic Measurement Integrated Simulation, Blood Flow, Ultrasonic Measurement, In Vitro Validation, PVA-H

1. Introduction

Cardiovascular disease is one of main causes of death in many countries, the number of fatalities tending to increase with advancing age. Because of our fast-aging society, this is a problem calling for immediate attention. Previous studies have reported cardiovascular diseases to be closely related to blood flow[1-5], and much research has been performed from

*Received 19 Dec., 2007 (No. 07-0839)
[DOI: 10.1299/jbse.3.161]

this point of view, most of which has been carried out by experimental measurement[6-10] (*in vitro* and *in vivo*) or, recently, by computational fluid dynamics (CFD).

Even with substantial improvement in measurement technology, it is still difficult to accurately measure the detailed structure of 3D blood flow, including the vessel wall shear stress and the wall pressure, important factors of cardiovascular diseases, by using existing measurement techniques, such as MRI, CT, X-ray, and ultrasonic measurement.

On the other hand, computer simulation of blood flow has also been actively conducted. A realistic solution of the blood flow can be obtained by solving the fundamental equations of the flow with realistic vessel geometry obtained by MRI or CT[9-13]. However, this method has inherent problems because it is generally difficult to accurately set boundary conditions of the blood flow and of the geometry of blood vessels, resulting in computational results that are sometimes insufficient to reproduce real blood flow.

This background indicates the necessity of finding a new way to obtain details on individual blood flow for treatment of patients suffering from cardiovascular disease and the need for fundamental research to uncover the causes of such disease. Our group has previously proposed a new method called Ultrasonic-Measurement-Integrated (UMI) simulation, in which ultrasonic measurement and CFD are integrated to reproduce blood flow[14]. UMI simulation is a kind of flow observer[15], the components of which are shown in Fig. 1. As shown in this figure, the ultrasonic measurement result is compared with the corresponding result of the numerical simulation, and the difference of the two is fed back to the numerical simulation as a feedback signal based on the feedback law to reduce the difference. By performing successive computation to reduce the difference to zero, the actual flow is reproduced asymptotically. In previous studies, Funamoto *et al.* confirmed the usability of UMI simulation by 2-D and 3-D numerical experiments with realistic geometry of a thoracic aneurysm[16-18]. Although these numerical experiments were performed based on the assumption that there is no measurement error in ultrasonic measurement, the result of actual ultrasonic measurement inevitably contains some measurement error. Since the accuracy of the ultrasonic measurement directly influences the accuracy of UMI simulation, evaluation and improvement of the measurement accuracy are essential to develop the UMI simulation system.

There are several modes of measurement in general medical ultrasonic instrument: B-mode, M-mode, pulse Doppler mode, power Doppler mode and color Doppler mode for corresponding examination purposes[19, 20]. In the color Doppler mode, in which the information on geometry and blood flow are available at the same time, the velocity component of the fluid along the ultrasonic beam is measured based on the Doppler shift frequency, and it is converted to the intensity of colors, namely, the color Doppler value, to visualize the blood flow. Generally, the velocities toward the ultrasound probe and those away from the probe are displayed in warm and cold colors, respectively. A number of investigations have been performed on the validation of ultrasonic measurement using the fluid flow phantom[21], the spring-type phantom[22], and the belt-type phantom[23].

Although the PC controlled spring-type phantom and the belt-type phantom provide steady Doppler signals, the experimental environments of these experiments are different from that

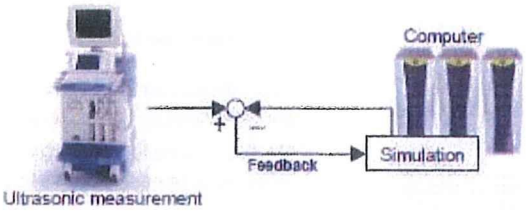

Fig. 1 Ultrasonic-measurement-integrated (UMI) simulation system

of the clinical use of ultrasonic measurement applying to the living tissue. On the other hand, the fluid flow phantom requires a complicated experimental setup, but the experimental environment is similar to that of the practical use of the ultrasonic measurement. In our previous study, we obtained the relationship between the color Doppler value and the Doppler velocity, abbreviated as "C-V relationship," by analyzing the color bar displayed on the monitor of the ultrasonic device[14]. In order to visualize the blood flow characteristics clearly, many signal conditioning schemes such as wall filters are equipped in commercial medical ultrasonic device. The evaluation of various filters as to simple input signals and measured Doppler signal samples have been performed in previous studies[24, 25]. However, it is difficult to apply the results of the previous studies to evaluate the effect of signal processing in a commercial medical ultrasonic device to be used in UMI simulation.

In this paper, we examined the accuracy of Doppler velocity measurement using a commercial medical ultrasonic diagnostic instrument as the measurement device. We developed an *in vitro* experimental system containing a poly (vinyl alcohol) hydrogel (PVA-H) fluid flow phantom, which we then employed for ultrasonic measurement. By measuring a fully developed laminar flow in a straight circular tunnel in the phantom, we investigated the C-V relationship in the ultrasonic measurement including the effect of several signal conditioning parameters. The effects of temporal and spatial averaging of ultrasonic measurement data were also discussed.

Nomenclature

C Color Doppler value ($0 \le C \le 255$, integer value)
D Diameter of the straight circular tunnel in PVA-H phantom
E Normalized error in Doppler velocity $(V - V_{ana})/V_{max}$
E_{ave} Average of E, $\frac{1}{y_2' - y_1'}\int_{y_1'}^{y_2'} E dy',\ y' = y/D,\ y_1 = 0.2D,\ y_2 = 0.8D$
f_{bright} Factor of brightness of B mode imaging
f_{cont} Factor of contrast of B-mode imaging in response to the color Doppler imaging
h Height of captured images
H Height of PVA-H phantom
L Length of PVA-H phantom
q Flow rate
r Position in the radial direction
Re Reynolds number, $\mathrm{Re} = U \cdot D/\nu$
U Mean flow velocity
$\vec{u}$ $\vec{u} = (u, v)$, flow velocity vector in cylindrical (z, r) coordinate system
u_{max} Maximum velocity in the flow direction
V Measured Doppler velocity (positive value corresponds to the direction toward the probe)
V_{ana} Analytic solution for the Doppler velocity
V_{max} Maximum value of the measured Doppler velocity
$V_{max,ave}$ Analytic Doppler velocity averaged over the cross section
V_0 Maximum Doppler velocity
w Width of captured images
W Width of PVA-H phantom
y Position in the diametral direction
z Position in the flow direction

Greek letters
φ Angle of ultrasonic beam emission
θ Angle between ultrasonic beam and flow direction

2. Materials and Methods

2-1 Experimental system

Figure 2 (a) shows an overview of the experimental system. Working fluid, namely, artificial blood (ATS Laboratories, model 707) consisting of water, glycerin, and tracking particles was driven by a constant head tank. The entry region of a straight PVC tube with a length of 2000 mm, a diameter of 10 mm, and a thickness of 1.5 mm, was positioned to ensure a fully developed laminar flow in the PVA-H phantom, a block ($L \times W \times H$ = 500 mm × 70 mm × 50 mm) with a straight circular tunnel having a diameter of 10 mm. Connectors were placed at the both ends of the tunnel. Details of the PVA-H phantom are explained in the next section. We used a commercial medical ultrasonic diagnostic device (TOSHIBA, SSA-700A). A linear scanning probe (TOSHIBA, PLT-704AT 7.5 MHz) employed for ultrasonic measurement was applied at a position 400 mm from the entrance of the phantom. Figure 2 (b) shows the definition of the angles, namely, the entry angle of the ultrasonic beam, φ, and the angle between the ultrasonic beam and the flow velocity, θ. The beam entry angle φ was set at 70° and 110° corresponding to the angle between the ultrasonic beam and the flow velocity θ of −70° and −110°, respectively. The flow rate was measured by a flowmeter (ATS Laboratories, model 752) and controlled by a flow control valve downstream of the circuit. Figure 3 shows the PVA-H phantom and the ultrasonic probe. The experimental conditions are shown in Table 1.

2-2 PVA-H phantom

Poly (vinyl alcohol), PVA, is widely used as an industrial compound, a biomedical medium, and material for food packaging. PVA and the water solution can be easily levigated, and phantoms made of PVA hydrogel (PVA-H) have been used in some previous studies[26-28]. PVA-H is a tissue-mimicking material. Compared with conventional phantoms made of silicone rubber or acrylic plastic, PVA-H phantoms are characterized by elasticity and low skin friction due to their high moisture content[26]. This high moisture content also means that PVA-H phantoms have an acoustic impedance near that of the living body, and thus enabling ultrasonic measurement[27, 28]. The elasticity of the PVA-H can be adjusted in a wide range with PVA of appropriate weight in the water solution; for example, 5% PVA-H has almost the same Young's modulus as the liver[26].

Commercial PVA powder (JAPAN VAM & POVAL, JF-17) was used to make the phantom employed in this study. We made 10 wt% PVA liquid with 300 g of PVA powder and 2700 g of solvent, which was a mixture of 20 wt% water and 80 wt% DMSO (Dimethylsulfoxide). PVA powder was dissolved in the solvent at 120℃ for 120 minutes. After the dissolution, PVA liquid was cast in a stainless box ($L \times W \times H$ = 500 mm × 70 mm × 50 mm) through which an aluminum cylindrical bar (D = 10 mm) and two connectors were set.

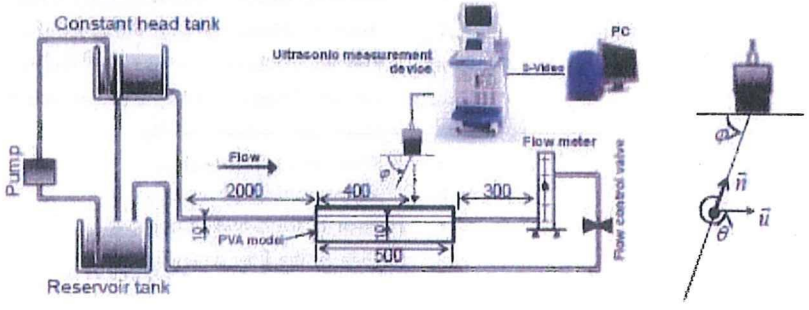

(a) (b)

Fig. 2 (a) Overview of experimental system and (b) definition of angles

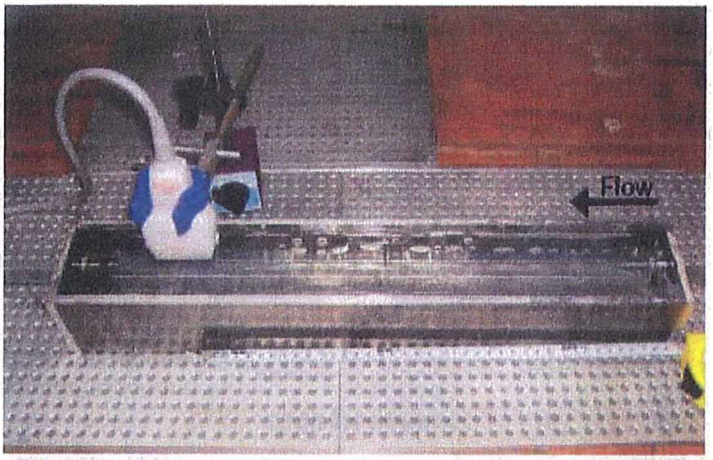

Fig. 3 PVA-H phantom and ultrasonic probe at the measurement position

Table1 Experiment conditions

Angle of ultrasonic beam emission, φ	70°, 110°
Angle between ultrasonic beam and flow velocity, $\theta(-180^\circ \le \theta \le 180^\circ)$	-70°, -110°
Center frequency	7.5 MHz
Pulse repetition frequency	8.5 kHz
Measurement range, V_o	9.0 cm/s
Brightness of B-mode imaging, f_{bright}	60, 80 (default)
Contrast of color Doppler imaging and B-mode imaging, f_{cont}	14 (default), 15
Density of working fluid	1040 kg/m^3
Kinematic viscosity of working fluid	1.66×10^{-6} m^2/s
Picture capture rate	16 Hz
Pixel size	0.05208 mm/pixel

After cooling the PVA solvent to room temperature, the solvent in the box was placed in a freezer at −30 ℃ for 24 hours for gelation. We obtained a PVA-H straight tube fluid flow phantom by pulling out the aluminum bar after the gelation.

2-3 Method to investigate the C-V relationship

The experiment was performed at a flow rate ranging from 1.57×10^{-6} m^3/s to 1.16×10^{-5} m^3/s, corresponding to Re = 75 - 886. As shown by Fig. 2 (a), the site of measurement was 40 D from the inflow of the phantom and there was an additional 200 D straight PVC tube in the upstream region. Therefore, the flow at the measurement position with the maximum Reynolds number Re = 886, corresponding to the flow rate q = 1.16×10^{-5} m^3/s and the mean velocity u = 0.148 m/s, was a fully developed laminar flow since the entrance length was theoretically estimated as $0.065\mathrm{Re}\,D = 58D$.

The color Doppler images ($w\times h$ = 720 pixels × 486 pixels) of the ultrasonic measurement were transferred to a graphic workstation (SGI, O2) by an s-video cable. We captured 100 contiguous images with a capture frequency of 16 Hz. The maximum Doppler velocity of the measurement range (V_o) of the ultrasonic instrument device was held at 9.0 cm/s. The measured Doppler velocity (V) ranged between 0.0 and 9.0 cm/s with $\theta=-70^\circ(\varphi=70^\circ)$, and −9.0 and 0.0 cm/s with $\theta=-110^\circ(\varphi=110^\circ)$. Color Doppler images were stored in SGI rgb format or IRIX rgb, which is the standard bitmap format used in the IRIX operation system.

The set of 100 images was transferred and processed in the server (SGI, Prism). The intensities of red, green, and blue at each pixel on the images were extracted by an original program. We obtained the temporal average of 100 images in the whole domain first, and then the spatial average in the flow direction (350 pixels). In previous studies[14], the relationship between the color Doppler value and the Doppler velocity (C-V relationship) was obtained by analyzing the color bar in the captured images (Fig. 4 (a)). Figure 4 (b) shows the C-V relationship obtained with the method employed in the previous study. The sign of the Doppler velocity was determined by comparing the color Doppler values of red and blue. The amplitude of the Doppler velocity was almost proportional to the color Doppler value of green.

In the present study, we obtained the C-V relationship by comparing the maximum value of green in each distribution of the color Doppler value with the corresponding velocity of the analytic solution.

2-4 Visual adjustment factor of ultrasonic instrument

Several visual adjustment factors are possible with the present ultrasonic instrument. Among them, two factors may influence the Doppler velocity measurement: the factor f_{bright} of the brightness of the B-mode imaging and the factor f_{cont} of the contrast of the B-mode imaging with respect to the color Doppler imaging. Since the effect of these factors on the velocity measurement was not clear, it was also investigated in this study.

The brightness factor f_{bright} may change from 60 to 100 in the present system. The B-mode image of the object is invisible on the monitor at $f_{bright} = 60$, and the intensity increases as the factor increases. The contrast factor f_{cont} may change from 0 to 15. Only the B-mode image is displayed for $f_{cont} = 0$, and the intensity of the color Doppler image increases as the factor increases. Figures 5 (a) and (b) show examples of the captured image at Re = 690 with $\theta = -70°$ and $f_{cont} = 14$ (default) with two different f_{bright} values. The default setting of the factor $f_{bright} = 80$ and $f_{cont} = 14$ are used hereafter.

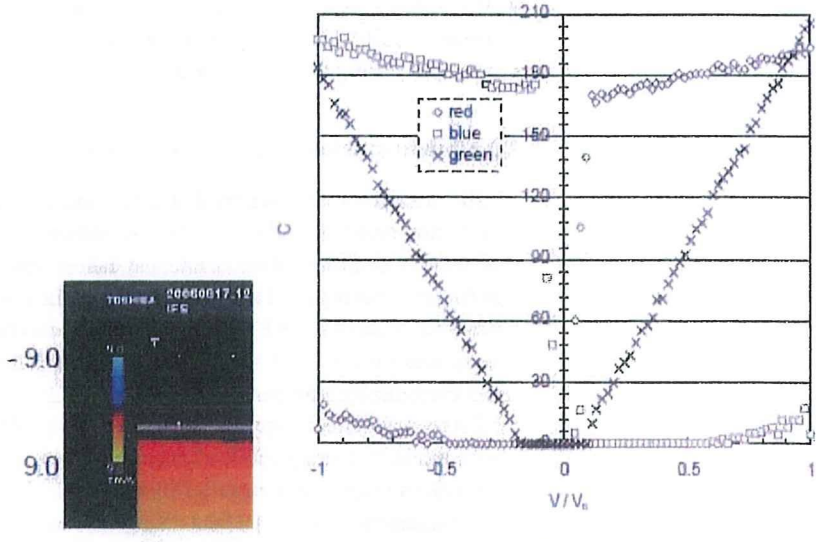

Fig. 4 (a) Color bar and (b) C-V relationship shown by the color bar

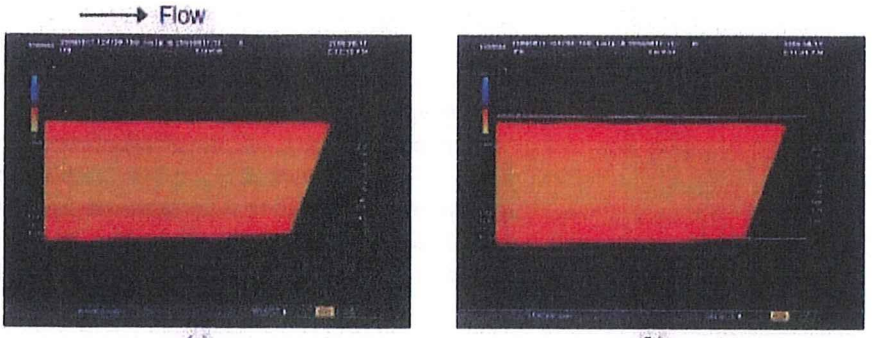

(a) (b)

Fig. 5 Color Doppler image for $q = 8.83 \times 10^{-6}\ \mathrm{m}^3/\mathrm{s}$, Re = 690, $\theta = -70°$, $f_{cont} = 14$ with (a) $f_{bright} = 60$ and (b) $f_{bright} = 80$ (default)

3. Results and Discussion

3-1 C-V relationship

The color Doppler image was obtained for the range of Reynolds number between Re = 75 and 860 for $\theta = -70°$, and between Re = 102 and 886 for $\theta = -110°$. Aliasing was observed for Reynolds numbers larger than the range for each beam θ. It should be noted that the maximum Reynolds number depends on the beam angle and is larger than that for the specified measurement range for $V_{max} = V_o$ (Re = 794 and $q = 1.03 \times 10^{-5}\ \mathrm{m}^3/\mathrm{s}$).

Figures 6 (a) and (b) show the distribution of the color Doppler value in the diametral direction at each flow rate for $\theta = -70°$ and $\theta = -110°$, respectively. It should be noted that each result was obtained from 100 sequential images by averaging in time and then averaging in space in the axial direction. The distributions of the color Doppler value are not parabolic, which implies that the former linear C-V relationships are not valid.

By comparing the maximum color Doppler value with the maximum velocity of the analytic solution at the center for each case, we obtained the C-V relationship shown by the symbols ○ and × in Fig. 7 for the B-mode contrast factors f_{cont} = 14 (default) and 15, respectively. C-V relationships for $\theta = -70°$ and $\theta = -110°$ are different but are both nonlinear. There is little difference between the results with f_{cont} = 14 and 15, so we deal with the case of f_{cont} = 14 (default) in the following.

We obtained the polynomial function to approximate each C-V relationship as

$$V/V_o = -3.32 \times 10^{-12} \cdot C^6 + 1.65 \times 10^{-9} \cdot C^5 - 3.09 \times 10^{-7} \cdot C^4 + 2.65 \times 10^{-5} \cdot C^3 - 9.75 \times 10^{-4} \cdot C^2 + 1.74 \times 10^{-2} \cdot C \quad \text{for} \quad \theta = -70° \tag{1}$$

$$V/V_o = -4.57 \times 10^{-9} \cdot C^4 + 1.50 \times 10^{-6} \cdot C^3 - 1.49 \times 10^{-4} \cdot C^2 - 3.82 \times 10^{-3} \cdot C \quad \text{for} \quad \theta = -110°$$

The solid lines in Fig. 7 based on Eq. (1) agree well with the measurement data. The broken lines in Fig. 7 are based on the approximate functions obtained from the green data of the color bar in Fig. 4 (b) as

$$V/V_o = 4.51 \times 10^{-3} \cdot C + 0.067 \quad \text{for} \quad \theta = -70°$$
$$V/V_o = -4.53 \times 10^{-3} \cdot C - 0.17 \quad \text{for} \quad \theta = -110° \tag{2}$$

The present C-V relationships (Eq. (1)) are different from the ones obtained from the color bar (Eq. (2)).

We converted measured color Doppler values to Doppler velocities with both of the C-V relation functions. Figure 8 shows an example for the converted Doppler velocity

distributions for $\theta = -70°$ and $\theta = -110°$ at Re = 690 compared with the analytic solutions. The velocity distributions based on the present C-V relationships agree with the analytic solutions except in the region near the wall, while those with the former C-V relationships do not agree in the whole region.

The influence of f_{bright} on the Doppler velocity measurement is shown in Fig. 8 for $\theta = -70°$. The result of $f_{bright} = 60$ is essentially the same as that of $f_{bright} = 80$ (default) showing good agreement with the analytical solution except in the region near the tube walls. Doppler velocity measurement with $f_{bright} = 60$, which is free from the influence of B-mode imaging, does not improve the accuracy of velocity measurement near the wall.

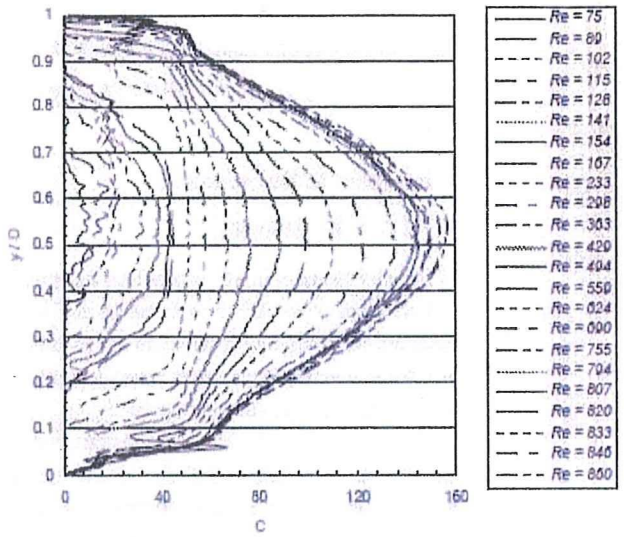

(a)

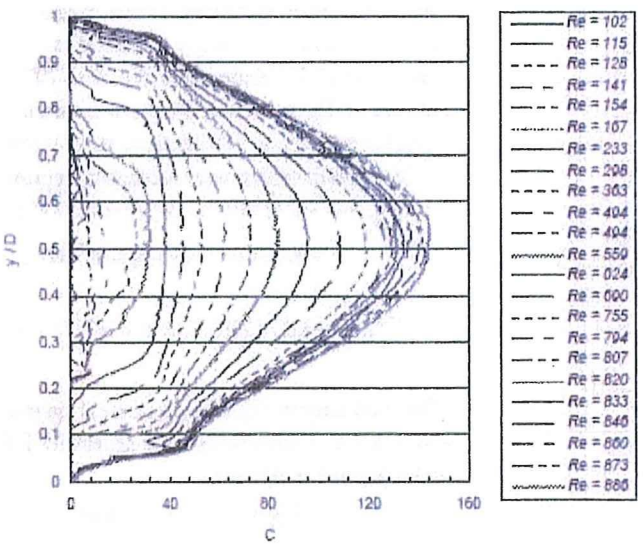

(b)

Fig. 6 Distribution of the color Doppler value in the diametral direction with $f_{cont} = 14$, $f_{bright} = 80$ for (a) $\theta = -70°$ and (b) $\theta = -110°$

These results suggest the possibility that the measurement data near the wall should be removed from the feedback signal of UMI simulation. In addition, the technique to extract the vessel boundary from the color Doppler image is an important problem, but is beyond the scope of the present paper.

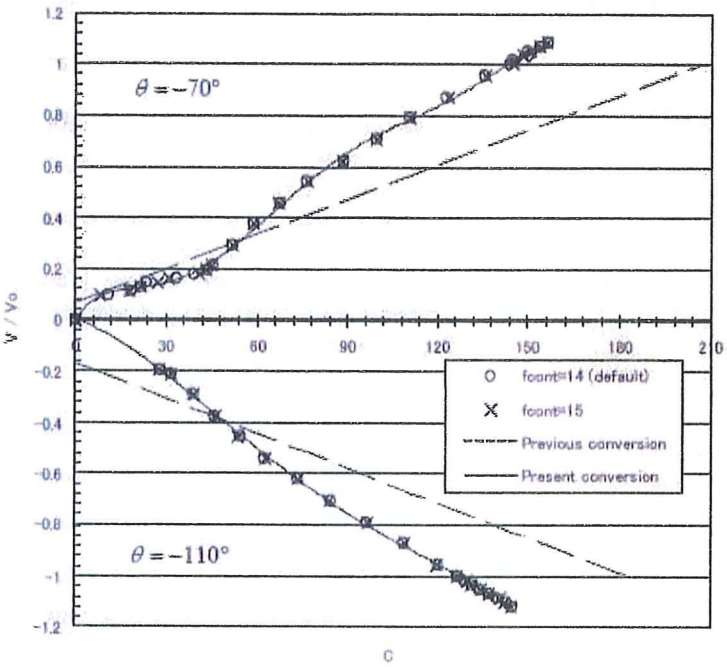

Fig. 7 Comparison of C-V relationships and conversion functions

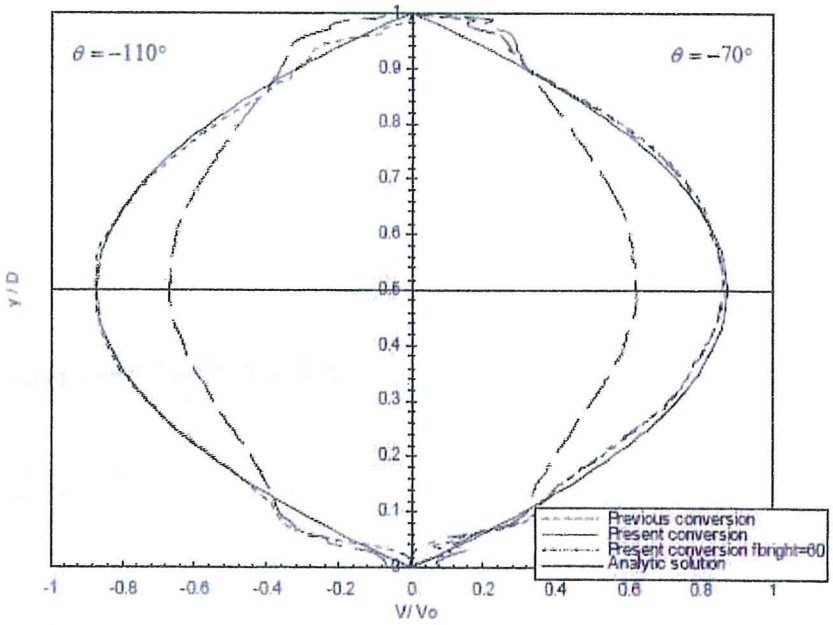

Fig. 8 Comparison of converted Doppler velocities (Re = 690)

3-2 Accuracy of ultrasonic measurement

Figures 9 (a) and (b) show the normalized error E in Doppler velocity along the diameter for various Reynolds numbers with the beam angles $\theta = -70°$ and $\theta = -110°$, respectively. The normalized error is defined as

$$E = \frac{V - V_{ana}}{V_{mean}}, \tag{3}$$

where V_{ana} is the analytic solution for the Doppler velocity and V_{mean} is the average value of V_{ana}. The error is relatively large in the case of low Reynolds number, as well as in the region near the wall.

Figure 10 shows the distribution of the normalized error E with the Reynolds number for representative points along the diametral direction. The figure shows that the relative error is larger for small Doppler velocities. It is noted that the relative error near the tube wall (broken lines) is larger than that near the tube axis (solid lines) in the region of small Doppler velocities.

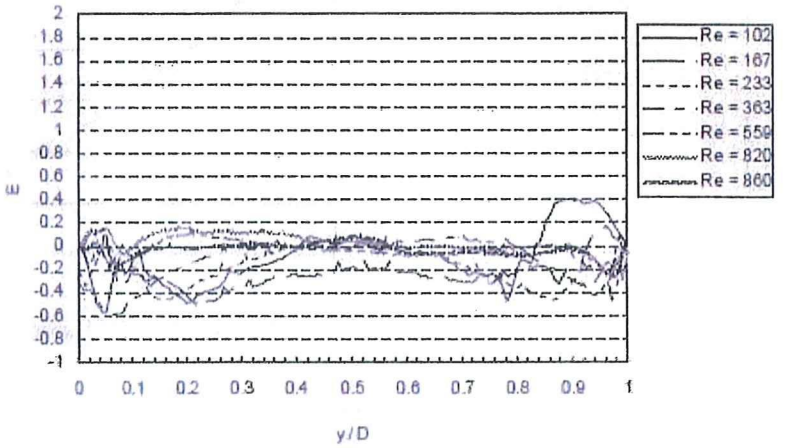

(a)

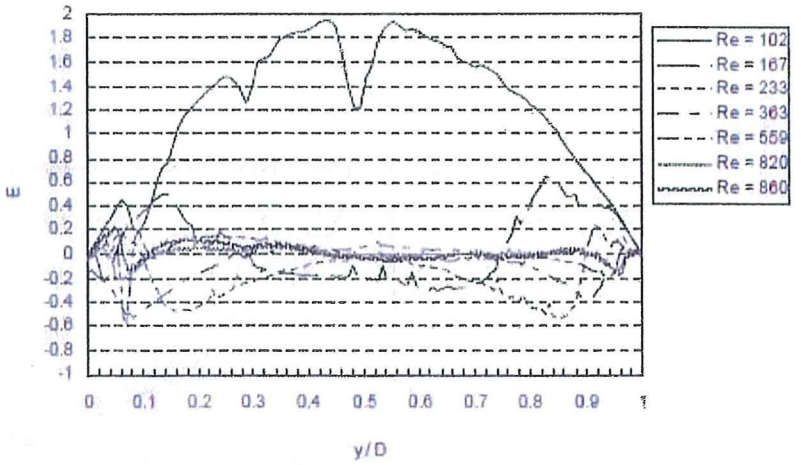

(b)

Fig. 9 Normalized error in Doppler velocity in the diametral direction for various Re with (a) $\theta = -70°$ and (b) $\theta = -110°$

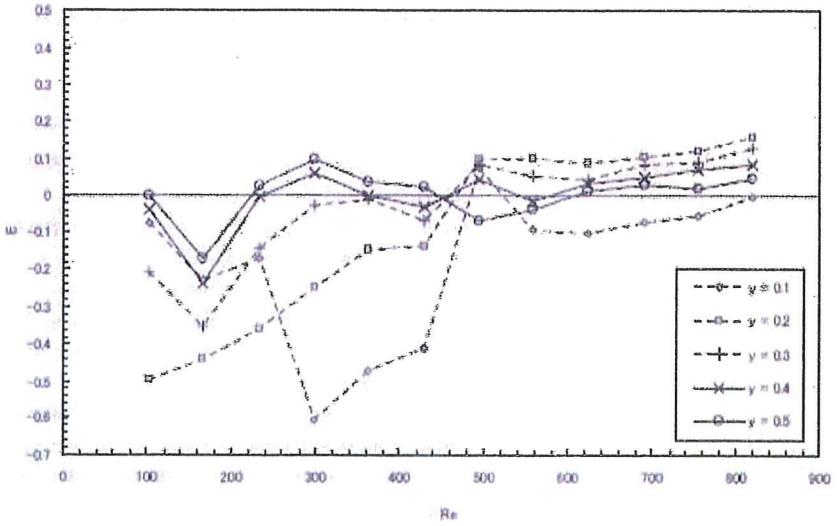

Fig. 10 Normalized error with Reynolds number at representative points in the diametral direction ($\theta = -70°$)

Based on the above results, Fig. 11 shows the normalized error E_{ave} averaged in the region near the center of the tube between 0.2 D and 0.8 D in the diametral direction. With increasing Reynolds number, the relative error first decreases and then remains almost constant below 10% for the Reynolds numbers larger than 500.

From the above examination, we confirmed that the measurement results converted with the proposed C-V relationships are reliable for high Reynolds number cases but that the results near the wall contain much measurement error compared with those near the center of the tube. In order to perform the UMI simulation precisely, the experimental data fed back to the numerical simulation should be as precise as possible. Thus, these results suggest that the precise part of the measurement data obtained with an appropriate setting for the range V_n of Doppler velocity measurement be used for feedback.

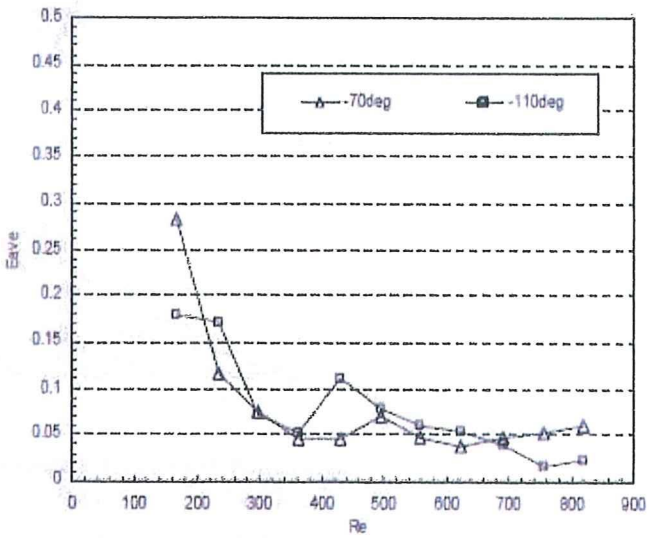

Fig. 11 Averaged normalized error with Reynolds number

3-3 Temporal and spatial averaging of ultrasonic measurement data

As noted in the above-mentioned examination, the ultrasonic measurement data averaged both temporally and spatially reproduce the velocity distribution of a steady laminar flow correctly except in the region near the tube wall. However, actual blood flow changes in time and space. Therefore, the number of data to take an average is limited to ensure appropriate spatial and temporal resolutions. On the other hand, reducing the number of data for averaging increases the effect of measurement noise. In this section, we examine the effect of temporal and spatial averaging of the ultrasonic measurement.

Figure 12 shows the distribution of the Doppler velocity for $\mathrm{Re} = 690$ and $\theta = -70°$ at one cross section temporally averaged using different numbers of sequential data ranging from 1 to 100 images. Increasing the number of averaging data results in closer agreement with the analytic solution.

Figure 13 shows the result at one point of time spatially averaged using different numbers of neighboring data ranging from 1 to 300 pixels. Similar to the former case, increasing the number of spatial averagings results in better agreement with the analytic solution.

Finally, we investigated the decrease of error in relation to the number of temporal and spatial averagings. We evaluated the decrease of the error E_{uw} in relation to the increase in the number of temporal averaging data for 6 cross-sections 2.604 mm apart and in relation to the number of spatial averaging data for 6 points of time at intervals of 1.25 s. Figure 14 shows that the error monotonically decreases with an increase in the number of averaging data. For example, an error of 5% was achieved by temporal averaging with 20 data at time intervals of 1.25 s or by spatial averaging of 50 data for an axial length of 2.604 mm. A combination of temporal and spatial averaging would possibly further reduce the error. The above results are essential for evaluation of the accuracy and resolution of the UMI simulation of real blood flow.

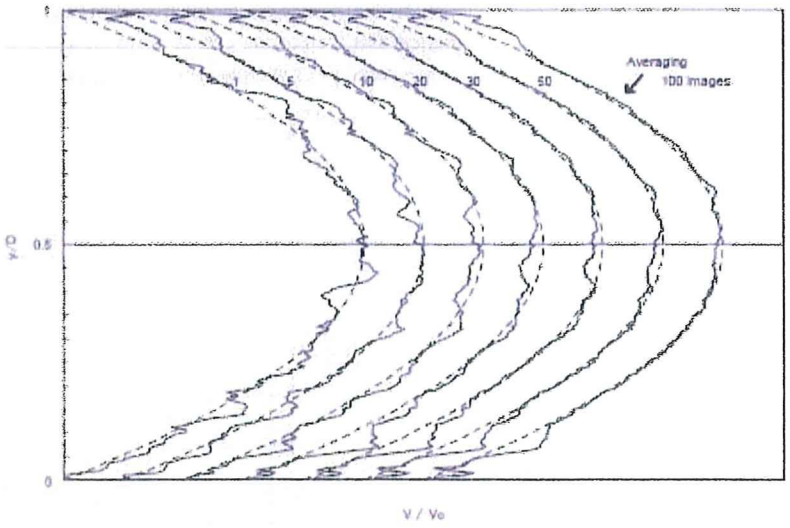

Fig. 12 Effect of temporal averaging at one cross section ($\mathrm{Re} = 690, \theta = -70°$)
Broken lines and solid lines show the analytic solution of V / V_o and its converted results, respectively.

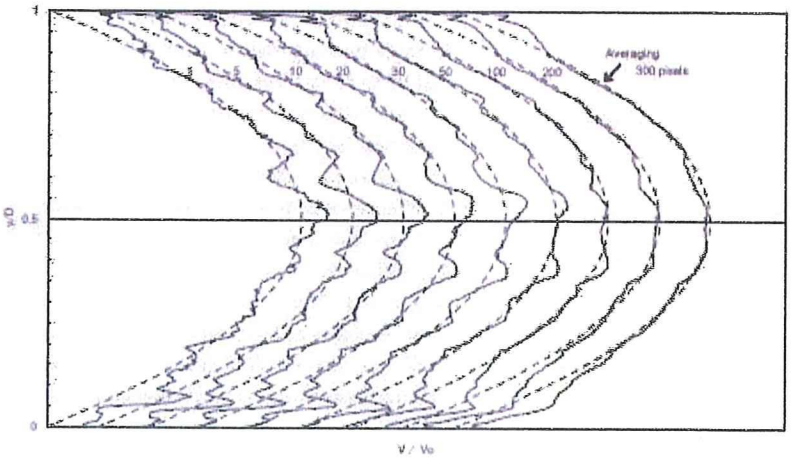

Fig. 13 Effect of spatial averaging at one point of time ($\mathrm{Re} = 690, \theta = -70°$)

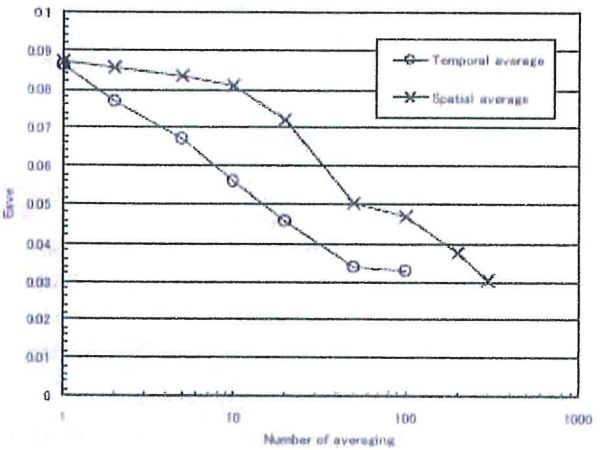

Fig. 14 Averaged normalized error with the number of temporal or spatial averagings ($\mathrm{Re} = 690, \theta = -70°$)

4. Summary

In this study, we performed ultrasonic measurement with a PVA-H fluid flow phantom as a fundamental study for experimental validation of Ultrasonic-Measurement-Integrated (UMI) simulation.

We developed an experimental system utilizing a PVA-H phantom. By measuring a developed laminar flow through a straight circular tunnel inside the phantom and analyzing the measured color Doppler images, we obtained a relationship between the color Doppler value and the Doppler velocity. This C-V relationship was confirmed at two angles between the ultrasonic beam and the flow velocity, $\theta = -70°$ and $\theta = -110°$. The velocity distribution converted from the present C-V relationships showed far better agreement with the analytic solution than that converted from the C-V relationships obtained by the color bar. The investigation of the normalized error E confirmed that the result obtained with the present C-V relationships was reliable for relatively high Reynolds numbers, but that the accuracy near the wall was somewhat degraded.

Investigation of the influences of two signal conditioning factors, namely, the brightness of B-mode imaging and the contrast of color Doppler imaging and B-mode imaging showed that these factors had little effect on the velocity measurement results.

Furthermore, we investigated the effect of temporal and spatial averaging of ultrasonic measurement data as a fundamental consideration of the UMI simulation of real blood flow. In both temporal and spatial averaging, increasing the number of averaging data resulted in a better agreement with the analytic solution.

The results obtained in this paper confirmed that a commercial medical ultrasonic device is applicable in a flow domain except near the wall by properly evaluating the C-V relationship. It was suggested that setting an appropriate measurement range for the blood flow condition and appropriate temporal averaging of the measurement data would result in UMI simulation with high accuracy. Based on these results, experimental validation and a trial application of real UMI simulation will be conducted in the future.

Acknowledgement

The authors acknowledge the support received from the Future Medical Engineering Based on Bio-nanotechnology Program (21 COE Program) and the Global COE Program "Global Nano-Biomedical Engineering Education and Research Network Centre." The signal processing was performed on the Integrated Supercomputing System in the Advanced Fluid Information Research Center, Institute of Fluid Science, Tohoku University.

References

[1] Fry DL: Acute Vascular Endothelial Changes Associated with Increased Blood Velocity Gradients. *Circulation Research*, Vol. 22, No.2, (1968), pp. 165-197.

[2] Reidy MA, Bowyer DE: Scanning Electron Microscopy of Arteries. The Morphology of Aortic Endothelium in Haemodynamically Stressed Areas Associated with Branches. *Atherosclerosis*, Vol. 26, No. 2, (1977), pp. 181-194.

[3] Caro CG: Mechanical Factors in Atherogenesis. In: Hwang NHC, Norman NA, eds. Cardiovascular flow dynamics and measurements. *Baltimore: University Park Press*, (1997), pp. 473-487.

[4] Zarins CK, Giddens DP, Bharadvaj BK, Sottiurai VS, Mabon RG, Glagov S: Carotid Bifurcation Atherosclerosis. Quantitative Correlation of Plaque Localization with Flow Velocity Profiles and Wall Shear Stress. *Circulation Research*, Vol. 53 (1983), pp. 502-514.

[5] Ku DN, Giddens DP, Zarins CK, Glagov S: Pulsatile Flow and Atherosclerosis in the Human Carotid Bifurcation. Positive Correlation Between Plaque Location and Low Oscillating Shear Stress. *Arteriosclerosis*, Vol. 5, (1985), pp. 293-302.

[6] Krueger JW, Young DF, Cholvin NR: An in vitro Study of Flow Response by Cells. *Journal of Biomechanics*, Vol. 4, (1971), pp. 31-36.

[7] Remuzzi A, Dewey CF, Davis PF, Gimbrone MA, Jr: Orientation of Endothelial Cells in Shear Fields in vitro. *Biorheology*,Vol. 21, (1984), pp. 617-630.

[8] Flora HS, Talei-Faz B, Ansdell L, Chaloner JE, Sweeny A, Grass A, Adiseshiah E: Aneurysm Wall Stress and Tendency to Rupture Are Features of Physical Wall Properties: an Experimental Study. *Journal of Endovascular Therapy*, Vol. 9, (2002), pp. 665-675.

[9] Papathanasopoulou P, Zhao S, Köhler U, Robertson MB, Long Q, Hoskins P, Xu XY, Marshall I: MRI Measurement of Time-resolved Wall Shear Stress Vectors in a Carotid Bifurcation Model, and Comparison with CFD Predictions. *Journal of Magnetic Resonance Imaging*, Vol. 17, No. 2, (2003), pp. 153-162.

[10] Marshall I, Zhao S, Papathanasopoulou P, Hoskins P, Xu XY: MRI and CFD Studies of Pulsatile Flow in Healthy and Stenosed Carotid Bifurcation Models. *Journal of*